Volume 28
Number 12
25 March 2026
Pages 7237–7810

PCCP

Physical Chemistry Chemical Physics

rsc.li/pccp

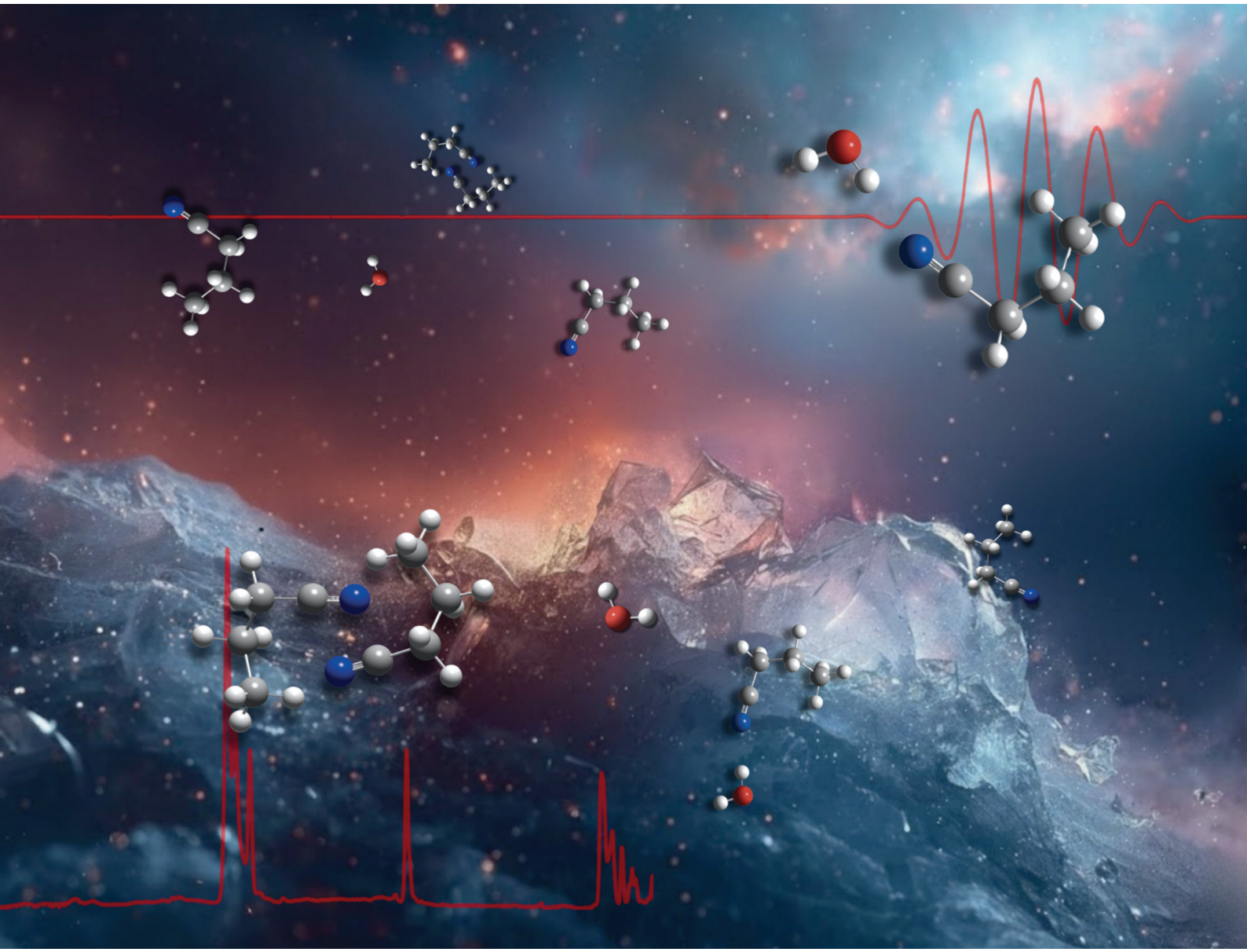

ISSN 1463-9076

ROYAL SOCIETY OF CHEMISTRY

PAPER

B. M. Broderick *et al.*

Water-mediated conformer-selective desorption of *n*-propyl cyanide from mixed ices

PCCP Owner Societies

PCCP

PAPER

View Article Online
View Journal | View Issue

Cite this: *Phys. Chem. Chem. Phys.*, 2026, **28**, 7282

Water-mediated conformer-selective desorption of *n*-propyl cyanide from mixed ices

E. M. Hayden, T. J. Hager, R. Mata, Q. B. Borengasser and B. M. Broderick *

Complex molecules formed in astrophysical ices may exist as different conformers, yet conformer-specific desorption under interstellar medium-relevant conditions remains poorly constrained. This in turn may give rise to uncertainties that impact inferred column densities for these species. Nitrogen-bearing species are particularly advantageous targets to study these issues owing to their large dipole moments, and *n*-propyl cyanide (*n*-PrCN), the smallest cyanide exhibiting rotational isomerism, serves as a benchmark system for investigating conformer-dependent ice-gas phase evolution. Here, we report the first measurement of the conformer interconversion barrier of *n*-propyl cyanide in the condensed phase (2044.9 ± 289 K) obtained using *in situ* reflection–absorption infrared spectroscopy (RAIRS). Mixed *n*-PrCN:H_2O ices were also examined, yielding a significantly higher interconversion barrier for an 80 : 20 composition. In addition to *in situ* characterization of the ice, gas-phase detection of products is achieved with chirped-pulse mm-wave detection of molecules during temperature-programmed desorption, where neat *n*-PrCN ice produces a *gauche* fraction of 0.80 ± 0.03 in the gas phase. Conformer populations are tracked throughout ice warm-up and phase transitions. Finally, we find that crystallization of *n*-PrCN in mixed ices is suppressed until the onset of water ice crystallization, demonstrating that ice composition and morphology regulate desorption with conformer-specificity.

Received 31st December 2025,
Accepted 6th February 2026

DOI: 10.1039/d5cp05060j

rsc.li/pccp

Department of Chemistry, University of Missouri, Columbia, Missouri, 65203, USA. E-mail: broderickbm@missouri.edu

B. M. Broderick

Bernadette M. Broderick is currently an Assistant Professor in the Department of Chemistry at the University of Missouri, Columbia. She received her PhD from Wayne State University in Detroit, Michigan and completed her postdoctoral work at the University of Georgia. Her research program lies at the interface of physical chemistry and astrochemistry, with a focus on developing experimental approaches to probe the sublimation dynamics and energetic processing of ices under simulated interstellar conditions. Her work aims to elucidate the formation and evolution of complex organic molecules in space, as well as understand non-equilibrium dynamics over the course of thermal desorption.

1. Introduction

Cyanides, defined by the presence of a C≡N functional group, are widely employed as spectroscopic probes of molecular structure, dynamics, and kinetics owing to their large permanent dipole moments and strong coupling to electromagnetic radiation. Perturbations to the electron density of the nitrile bond are readily interrogated using vibrational spectroscopic techniques, such as Fourier-transform infrared (FTIR) spectroscopy in the mid-infrared region. In particular, the fundamental CN-stretching mode is highly sensitive to its local environment in the condensed phase, where frequency shifts arise from vibrational Stark effects and specific intermolecular interactions.[1,2] The magnitude and direction of these shifts provide direct insight into the electrostatic fields and noncovalent forces experienced by the molecule.

An astrochemically relevant environment in which such effects are pronounced is the entrapment of nitriles within hydrogen-bonded water ice networks. Previous experimental and theoretical studies have examined the influence of water on the CN stretching vibration for HCN and CH_3CN ices.[3,4] However, these investigations have largely been restricted to short chain cyanides. Although longer chain nitriles are less abundant than HCN and CH_3CN in the interstellar medium (ISM), several have been detected in the gas phase and are expected to

be present within interstellar ices through accretion and subsequent thermal processing.

One such molecule is *n*-propyl cyanide (*n*-PrCN, C_3H_7CN), which has been detected toward the Sagittarius B2 (Sgr B2) molecular cloud alongside its structural isomer *i*-propyl cyanide (*i*-PrCN).[5,6] *n*-PrCN exists as two low-energy rotational conformers, *gauche* and *anti*, differing in orientation of the –CN group relative to the CCC backbone. Each conformer possesses distinct vibrational signatures within the 650–4000 cm^{-1} spectral window, enabling simultaneous monitoring of conformer-specific vibrational modes, as well as the CN-stretch. This allows for *in situ* tracking of conformer populations as a function of ice temperature and composition during temperature programmed desorption (TPD).

In the solid state, *n*-PrCN exhibits several properties that are not observed in shorter-chain cyanides, arising from the combined effects of molecular flexibility and electronic interactions involving the nitrile group.[7,8] Most notably, condensed *n*-PrCN can form a molecular glass prior to crystallization. This kinetically trapped amorphous phase is characterized by enhanced molecular mobility and viscosity changes, leading to a metastable disordered structure that may be accessed from cooling from the liquid or by warming a vapor-deposited sample. Glass formation and subsequent crystallization have been extensively studied in materials and medicinal chemistry, particularly for aromatic and flexible molecular systems.[9–11] Upon further annealing, *n*-PrCN undergoes a final transition to a thermodynamically stable crystalline phase, which consists exclusively of the *gauche* conformer when formed from vapor-deposited ice.[12] The way in which water modifies these phase transitions and the resulting conformer distributions remains incompletely explored, despite its relevance to interstellar ice evolution.

At higher temperatures, crystalline *n*-PrCN ultimately desorbs into the gas phase, a process central to astrochemical models of ice sublimation in protostellar environments. Recent observations with the James Webb Space Telescope (JWST) have enabled the first tentative identification of CH_3CN and CH_3CH_2CN in interstellar ices *via* their strong mid-IR CN stretch vibration.[13] These observations allow for a direct comparison of ice-phase and gas-phase abundances of nitriles. However, a key question is whether sublimation preserves or modifies the conformer populations established in the condensed phase.

In SgrB2(N), an [*i*-PrCN]/[*n*-PrCN] ratio of 0.4 ± 0.06 has been derived from gas-phase observations.[6] While a conformer-specific detection of *gauche n*-PrCN has not yet been unambiguously established, Belloche *et al.* (2009) reported a tentative feature, albeit with baseline uncertainty and spectral blending. Assuming this feature represents a *gauche* detection, and accounting for uncertainty of the energy differences between *gauche* and *anti* conformers, the inferred *anti* to *gauche* ratio ranges from 0.51 : 0.49 (ΔE = 92 cm^{-1}) to 0.57 : 0.43 (ΔE = 117 cm^{-1}) at 150 K in Sgr B2(N).[5] These values highlight the sensitivity of the observed conformer ratios to both energetic parameters and thermal history.

In the condensed phase, water has been shown to alter isomerization barriers for a variety of molecular systems by modifying local potential energy landscapes.[14,15] However, experimental constraints on conformational isomerization involving the rotation of heavy (larger than hydrogen) molecular groups under astrochemical ice conditions remain scarce. To our knowledge, only a single study has directly examined this process. Hudson and Coleman investigated the temperature-dependent solid-state isomerization of cyclopropanecarboxaldehyde (C_4H_6O) in pure and water-rich amorphous ices.[16] They observed conformer relaxation toward the thermodynamically favored *trans* form upon warming from 14 K to 85 K, with complete conversion following crystallization. In mixed water ices, conformer ratios remained temperature dependent, though quantitative analysis was hindered by spectral overlap. Related behavior has been observed for 1,2-dichloroethane, where warming the solid led to an increase in the less stable *gauche* conformer, indicating that conformer populations in ices are governed by a complex interplay of kinetic, structural, and intermolecular effects rather than simple thermodynamic equilibration.[17]

In this work, we employ chirped-pulse mm-wave rotational spectroscopy (CP-mmW) in combination with reflection–absorption infrared spectroscopy (RAIRS) to investigate the influence of water on the *gauche* : *anti* conformer ratio of *n*-PrCN in both the condensed phase and the gas phase following thermal desorption. We apply our instrument CPICE (Chirped-Pulse Ice), which couples CP-mmW spectroscopy with buffer gas cooling, to obtain conformer-specific sublimation profiles during temperature programmed desorption. This is an extension of our previous study of pure *n*-PrCN ice to include water-rich ices enabling direct assessment of matrix effects on conformer-resolved binding energies.[18] The RAIRS spectra are used to track the *n*-PrCN conformer distribution during ice warmup. The changes in the frequency and intensity of the vibrational bands measured provides insight to the intermolecular forces the molecules experience during the various phase transitions. The temperature at which the *anti* conformer is depleted and the *gauche* conformer grows is used to quantify the condensed-phase isomerization barrier, the first measurement of this value for *n*-PrCN. Finally, the influence of water on the observed conformer ratio and its temperature dependence is investigated.

2. Experimental

The instrument used to carry out these experiments has been described in detail elsewhere.[19,20] Briefly, the CPICE apparatus consists of an ultrahigh vacuum (UHV, $\sim 1 \times 10^{-10}$ Torr) stainless steel chamber designed for the generation and spectroscopic study of molecular ices (Fig. 1). Gas-phase molecules are deposited onto a 1 cm × 1 cm silver substrate cooled to cryogenic temperatures to form an ice. The neat or mixed ices can be characterized *in situ* using RAIRS with FTIR detection in the condensed phase. In addition, temperature programmed desorption (TPD) experiments may be performed to bring the molecules into the gas phase for injection into a 20 K buffer gas

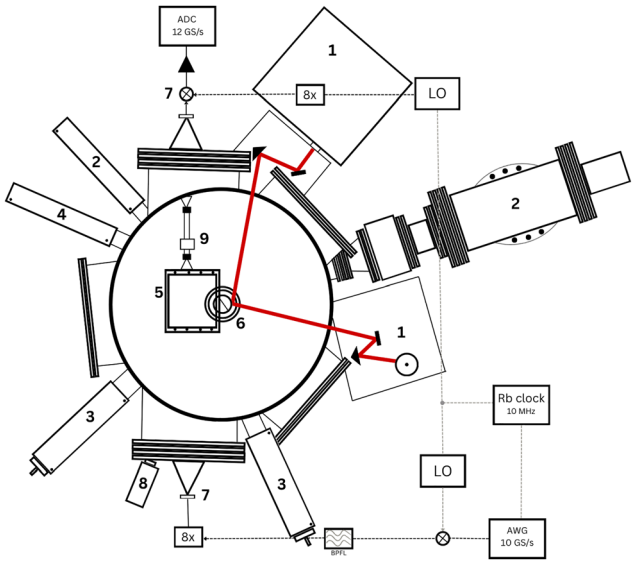

Fig. 1 CPICE instrumentation schematic showing its major components. 1: FTIR spectrometer 2: electron Gun/VUV Lamp 3: deposition lines 4: mass spectrometer 5: BGC 6: silver substrate 7: rotational spectrometer 8: HeNe Laser 9: Cryo-amp.

cell (BGC), where chirped-pulse mm-wave rotational spectroscopy is performed in the 60-90 GHz regime.

2.1. Ice generation

In the experiments described here, *n*-PrCN (Sigma Aldrich, $\geq$99%) was purified prior to deposition using three consecutive freeze–pump–thaw (FPT) cycles. The purified sample was warmed to room temperature and deposited through vapor phase deposition onto the silver substrate cooled to 5 K *via* a 4 K coldhead (Sumitomo RDK415D2-F70L) mounted to the bottom of the CPICE apparatus. For all experiments, the substrate temperature was maintained at 5 K during deposition. Ice thickness was monitored *via* laser interferometry using a 632.8 nm HeNe laser, allowing for accurate measurements at the nanometer scale.

For the mixed ice experiments, 18 MΩ resistivity water was deposited through a second deposition arm following three FPT cycles. Laser interferometry was used to monitor the thickness, while the ratio of the molecular components was monitored with a mass spectrometer throughout deposition to ensure the desired ratio remained constant. The column density of *n*-PrCN was held constant at approximately 3.97×10^{18} molecule cm^{-2}. The water was adjusted to match the column density of *n*-PrCN to achieve the different ratios used through the experiment. This leads to different ice thicknesses for each ice ratio: 5.7, 6, 7, 9, and 17 microns for pure, 80 : 20, 50 : 50, 25 : 75, and 10 : 90 respectively.

2.2. Temperature programmed desorption

Both *in situ* RAIRS measurements of the ice and gas-phase mm-wave measurements are performed over the course of TPD. A summary of the conditions employed in both detections schemes is provided below.

2.2.1. *In situ* RAIRS FTIR characterization. Following vapor deposition, ices were characterized *in situ via* RAIRS with a Thermo Nicolet iS20 FTIR spectrometer. For TPD experiments, the sample temperature was ramped at varying rates using a 50-Ohm cartridge heater (Lake Shore Cryotronics, HTR-50). Temperature was monitored by a silicon diode sensor (Lake Shore Cryotronics, DT-670C-BO-QT32–2, uncalibrated, ±1 K accuracy) mounted behind the substrate. Each RAIRS spectrum represents the average of 64 scans sweeping from 650–4000 cm^{-1} at a rate of 1.5 scans per second with a 4 cm^{-1} resolution. For neat ice experiments, a series of temperature ramping rates was employed to experimentally derive the barrier *for anti* → *gauche* rotational isomerization in the condensed phase. Ramping rates ranged from 0.2 K min^{-1} to 5 K min^{-1}. Infrared spectra were acquired at 5-min intervals for the slowest ramping rates and at 5 K temperature increments for the fastest ramps.

Quantitative determination of infrared band strengths in RAIRS is complicated by the combined effects of ice composition and temperature, both of which can substantially alter intrinsic (neat-ice) band strengths reported in the literature.[21,22] In water-rich ices, these effects are further complicated by optical interference inherent to the reflection–absorption geometry. Specifically, interference between photons reflected from the substrate and from the ice-reflected photons causes RAIRS peak areas to deviate from the linear column-density dependence expected under Beer–Lambert behavior.[23] These deviations are instrument-specific and depend sensitively on experimental parameters such as the grazing angle of the incident infrared beam.

RAIRS calibration experiments performed in CPICE demonstrate that departures from linearity of peak areas follow a cyclic pattern of constructive and destructive interference as a function of ice thickness. When a sufficiently broad range of ice thicknesses are sampled, a line-of-best-fit can be extracted that yields band strengths comparable to those obtained from transmission FTIR measurements, thereby avoiding bias toward any single phase of the interference cycle. We further observe that RAIRS interference effects are strongly frequency dependent, such that spectral features at widely separated frequencies exhibit distinct interference patterns. As a result, accurate comparison of bands separated by large frequency intervals would require frequency-specific corrections to the measured peak areas as a function of ice thickness.

In the present study, the vibrational bands selected for analysis are closely spaced in frequency and free from spectral overlap, minimizing RAIRS interference effects. Under these conditions, relative band areas can be compared reliably without the application of additional frequency-dependent corrections. Peak areas were measured using the Thermo Scientific OMNIC 9 program.

2.2.2. mm-wave Gas phase detection. In separate TPD experiments within CPICE, the lower ice stage is raised to the BGC maintained at 20 K by a closed-cycle He cryostat (Sumitomo RDK415D2-F70L) mounted to the top of the chamber to capture the mmWave spectra of the subliming molecules. Here, the temperature of the ice was ramped at a rate of 2 K min^{-1}.

Over the course of sublimation, the desorbing species enter the BGC where they are cooled through collisions with pre-cooled neon buffer gas (6 sccm). At the same time, a linear frequency sweep pulse from 84.04 GHz to 84.13 GHz captures four rotational transitions, the relative intensities of which were obtained by averaging up- and down-frequency sweeps using a 2 μs chirp duration and 12 μs listening time. Based on the measured T_2 coherence lifetimes, integration windows of 4 μs and 3 μs were applied for the *anti* and *gauche* conformers, respectively.

The transitions associated with each conformer were averaged to determine the overall *gauche* and *anti* relative abundances, *N*. Several corrections were applied in calculating these abundances as shown in eqn (1), including chirp corrected intensity *I*, conformer-specific partition functions Q_i, lower and upper state rotational energy contributions E_r'' and E_r', transition-specific signal line strength factors, $S\mu^2$, as governed by the experimentally measured rotational temperature of the desorbed molecules, as well as the lower state degeneracy g_1.

$$N_i \propto \frac{IQ_i}{vg_1\sqrt{S\mu^2}\left(e^{-\frac{E_r''}{kT_{rot}}} - e^{-\frac{E_r'}{kT_{rot}}}\right)} \quad (1)$$

A complete listing of all rotational transitions, their intensities at 18 K as reported in CDMS, and the corresponding line strength factors are provided in Table S2.[24] Further experimental details are described in greater depth in Borengasser *et al.*[25]

3. Results and discussion

3.1. *In situ* RAIRS characterization of neat *n*-PrCN ices

Neat *n*-PrCN deposited at 5 K forms an amorphous ice, as evidenced by broad infrared absorption features and the absence of crystalline splittings. Upon controlled thermal warm-up, the *in situ* RAIRS spectra reveal three distinct temperature regimes prior to sublimation, corresponding to amorphous, glassy, and crystalline morphologies as shown in Fig. 2. These regimes are reproducible across all temperature ramping rates explored in this study.

An important advantage of *n*-PrCN is the presence of clearly resolved infrared bands associated with individual conformers in the condensed phase. While a complete list of the condensed-phase spectrum is given in the Supplementary Information, Table S1, the bands of interest selected to understand the role of water in conformer composition within the ice are the 1260 cm^{-1} *gauche* band and the 1277 cm^{-1} *anti* band, both of which correspond to the $-CH_2$ twist in each species and which are spectrally distinct throughout the thermal evolution of the ice.[12] The integrated areas between 1270–1247 cm^{-1} and 1287–1270 cm^{-1}, respectively, were used to obtain the *gauche : anti* (*g : a*) ratio in all experiments.

Absolute conformer populations cannot be extracted without reliable conformer-specific band strengths, which are not available for *n*-PrCN under varying water concentrations and ice morphologies. Moreover, both ice temperature and matrix composition are known to modify intrinsic band strengths, while the reflection–absorption geometry introduces additional optical interference effects. As a result, all conformer ratios reported here are expressed relative to the 10 K *n*-PrCN reference spectrum, for which the *g : a* ratio is assumed to reflect the gas-phase equilibrium value (3 : 1) frozen in upon deposition at low substrate temperature, consistent with previous studies.[16,17] This approach enables accurate determination of the relative changes in conformer populations in the absence of absolute column densities.

Upon warming from 5 K to ~100 K, both conformer bands sharpen and increase in integrated intensity without a measurable change in their relative ratio (Fig. 2). This behavior indicates structural reorganization within the ice without conformer relaxation. Similar spectral sharpening has been previously associated with the formation of a metastable glassy state in flexible molecular solids, where increased mobility allows local rearrangements while long-range order remains absent.[26] Under our experimental conditions, this glass transition (T_g) occurs at 103–104 K (Fig. 3), slightly higher than the

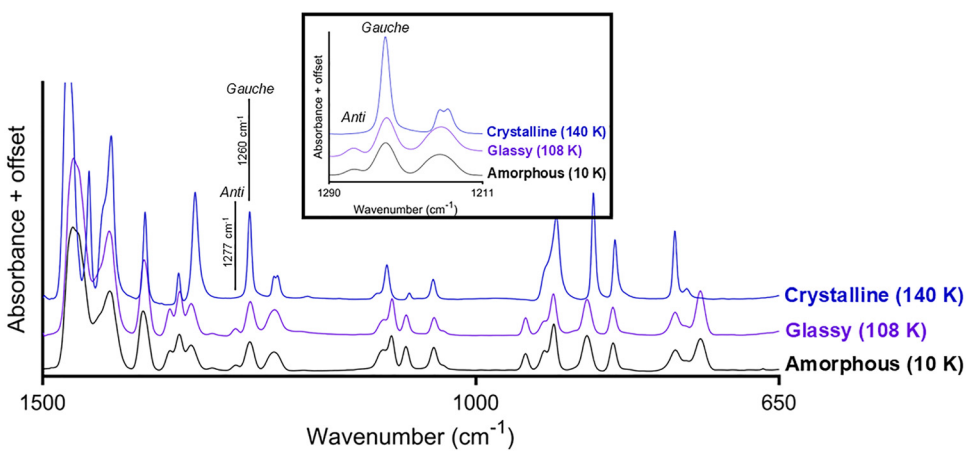

Fig. 2 RAIRS FTIR of pure *n*-PrCN at each observed ice phase in the IR region containing all the conformer-specific vibrational bands. The inset corresponds to the 1200 cm^{-1} region of the *anti* and *gauche* labeled CH_2 twist peaks.

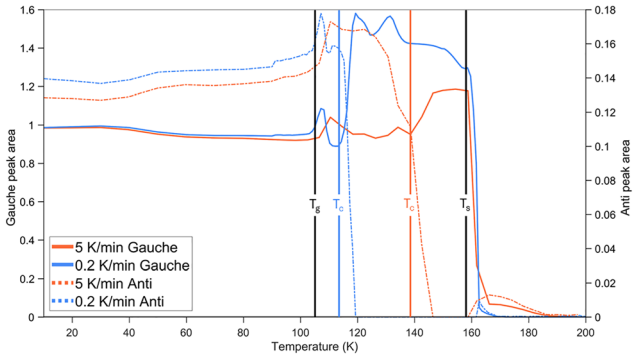

Fig. 3 Peak area of *gauche* and *anti* conformers measured over temperature at the lowest ramping rate (0.2 K min^{-1}) and the highest ramping rate (5 K min^{-1}) used for Kissinger analysis. The temperatures at which various transitions start are indicated (key: T_g = glass transition; T_c = crystal transition; T_s = sublimation).

97 K reported previously for *n*-PrCN under different deposition conditions,[7,27] consistent with the known sensitivity of glass formation to thermal history.[7]

Despite changes in band shapes and absolute intensities upon entering the glassy state, the *g : a* ratio remains consistent across all heating rates examined. This indicates that conformational interconversion is inhibited within both the amorphous and glassy states.

3.2. Crystallization induced-conformer interconversion in neat *n*-PrCN

Upon further heating, the ice undergoes crystallization, as indicated by the depletion of the *anti* conformer and simultaneous growth of the *gauche* species. This transition is accompanied by the appearance of multiple peak splittings and sharpening of non-conformer specific –CH vibrational features, consistent with the formation of a long-range ordered crystalline lattice. The final crystalline phase consists exclusively of the *gauche* conformer, in agreement with previous structural studies of vapor-deposited *n*-PrCN.[12] We did not have IR spectra in our previous examination of neat *n*-PrCN ice, so we were unable to monitor these effects.

Although the onset temperature of the glassy state is independent of heating rate, the temperature window within which this state persists prior to crystallization does depend on the ramping rate. At the slowest heating rate (0.2 K min^{-1}), the glassy state spans 15 K, whereas at the fastest heating rate (5 K min^{-1}), it extends over ~26 K. This rate dependence suggests that crystallization and conformer interconversion are kinetically coupled processes that require sufficient time for large-scale molecular rearrangement.

The absence of conformer relaxation prior to crystallization for *n*-PrCN ices is in contrast to the previously observed behavior by Ishii *et al.* for 1,2-dicholoroethane (DCE), where the higher-energy *gauche* conformer increases in abundance upon warming before crystallization.[17] In DCE, electrostatic interactions stabilize the polar *gauche* conformer in the condensed phase, lowering the effective rotational barrier relative to *n*-PrCN. The lack of analogous behavior here indicates that the barrier to C–C bond rotation in *n*-PrCN is higher than the barrier associated with chloromethyl group rotation in DCE, precluding conformer equilibration prior to crystallization.

3.3. Effective barrier height for condensed-phase conformer interconversion

Given the strong dependence of the crystallization-associated conformer transition on heating rate, we report an effective activation energy using the Kissinger method, which has been previously applied to quantify the kinetics of thermally stimulated processes in various materials.[28,29] For each ramping rate, the temperature of peak *anti* → *gauche* interconversion was identified from the conformer-peak area evolution as shown in Fig. 3. Applying the Kissinger relation,

$$E = -\frac{\mathrm{d}\ln\left(\frac{\beta}{T_p^2}\right)}{\mathrm{d}T_p^{-1}} \quad (2)$$

where β is the heating rate, and T_p is the temperature of maximum rate of interconversion, which yields and effective activation energy of 2044.9 ± 289 K for neat *n*-PrCN (Fig. 4).

We note that the crystallization and isomerization processes are intertwined kinetically, as both processes are measured using the changes in the peak areas of the conformers. As a result, the experimentally derived activation energy is that of a multi-step process and the value obtained from this simplified kinetic analysis serves as an upper bound on the true energy barrier for conformer isomerization. Nevertheless, this measurement provides the first experimental constraint on conformational dynamics of *n*-PrCN in the condensed phase.

For comparison, gas-phase calculations yield an *anti* → *gauche* barrier height of 1736.4 K at the CCSD(T)-F12 level of theory.[30] The modest increase observed in the condensed phase is consistent with previous studies demonstrating higher rotational barriers to interconversion in condensed environments due to intermolecular interactions and restricted molecular mobility. Analogous behavior has been reported for amide

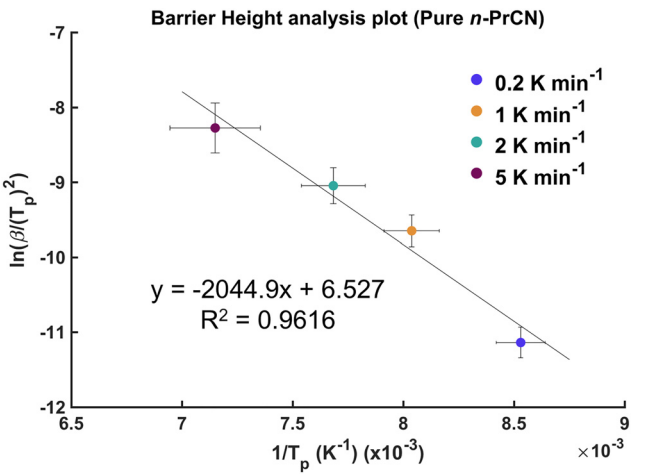

Fig. 4 Kissinger plot of *anti*-*gauche* interconversion barrier for pure *n*-PrCN ices.

bond rotation, where barriers increase from gas phase to neat liquids and further in hydrogen-bonded solutions.[31,32]

3.4. Effect of water on conformer interconversion and crystallization

To assess the influence of water on conformational dynamics, RAIRS spectra were collected for *n*-PrCN:H_2O mixed ices over a range of compositions during TPD. Fig. 5 below shows spectra for an 80 : 20 mixture, where the amorphous-to-glassy transition occurs without any measurable change in conformer ratio, as was observed in the neat ice. However, the crystallization behavior is notably different in the presence of water.

Plots showing integration of these RAIRS peaks for neat and 80 : 20 ices are shown in Fig. 6. For the 80 : 20 mixture, only the slowest heating rate (0.2 K min^{-1}) results in complete conversion to the *gauche* conformer, *i.e.* crystallization. At faster rates (1 and 1.5 K min^{-1}), crystallization remains incomplete and the *anti* conformer is present up to the point of desorption. This suggests that water significantly increases the timescale required for both structural ordering and conformer interconversion. Application of the Kissinger analysis to the slow-rate data yields an effective barrier height of ~7800 K for the mixed ice. Although this value may not directly reflect the barrier in this case, its magnitude suggests that hydrogen-bonding interactions with water strongly hinder intramolecular relaxation. The delayed onset of *n*-PrCN crystallization relative to the neat ice further indicates that *n*-PrCN ordering is coupled to water crystallization, consistent with previous observations of molecular segregation in mixed astrophysical ices.[21]

3.5. Water-perturbed CN stretching mode

A prominent spectral signature of *n*-PrCN-H_2O interactions is the appearance of a blue-shifted CN stretching band upon addition of water, as shown in Fig. 7 below. In pure *n*-PrCN, the strongest CN stretching mode appears at 2247 cm^{-1}. In mixed ices, a new band appears at 2260 cm^{-1} and becomes dominant even at low water fractions. This feature is assigned to the CN stretch perturbed by hydrogen bonding between the nitrile nitrogen and surrounding water molecules. Such blue shifts have been reported previously for acetonitrile in liquid solutions and solid matrices, where hydrogen bonding reduces electron density on the nitrogen atom, shortens the CN bond length, and increases its force constant.[1,3] Similar perturbed bands have been observed in MeCN:H_2O ices and used to quantify the hydrogen-bonding fractions as a function of temperature.[33]

To understand the frequency shifts observed in this work, Gaussian calculations were performed at the B3LYP/aug-cc-pVDZ level of theory. Harmonic vibrational frequencies were computed for an isolated *n*-PrCN molecule and for a *n*-PrCN-H_2O complex, in which the water –OH group is oriented toward the nitrile nitrogen. This configuration serves as a minimal model for hydrogen bonding in mixed *n*-PrCN-H_2O ices. Comparison of the calculated CN stretching frequencies reveals a blue shift of 13 cm^{-1} upon complexation with water relative to the isolated molecule. This calculated shift is in agreement with the experimentally observed blue shift of 13 cm^{-1} (Fig. S8).

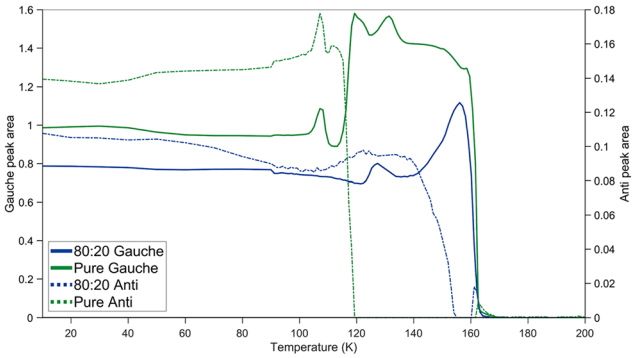

Fig. 6 Peak area of the *gauche* and anti conformer CH_2 twist mode measured over temperature for the 0.2 K min^{-1} ramping rate of the pure (green) and mixed ices (blue).

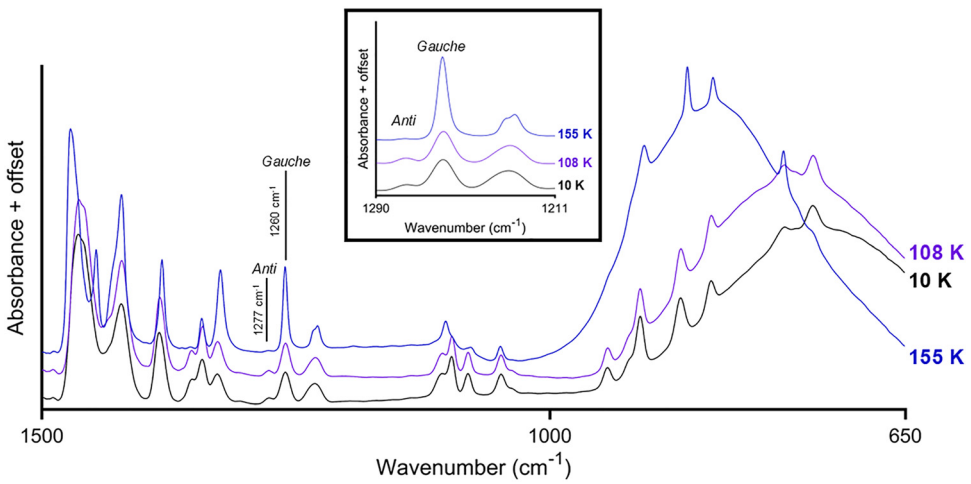

Fig. 5 RAIRS FTIR spectra of a 6 micron 80 : 20 PrCN:H_2O mixed ice at temperatures corresponding to possible ice phase transitions in the IR region showing all the conformer-specific vibrational bands. The inset corresponds to the 1200 cm^{-1} region of the anti and *gauche* labeled CH_2 twist peaks monitored during TPD.

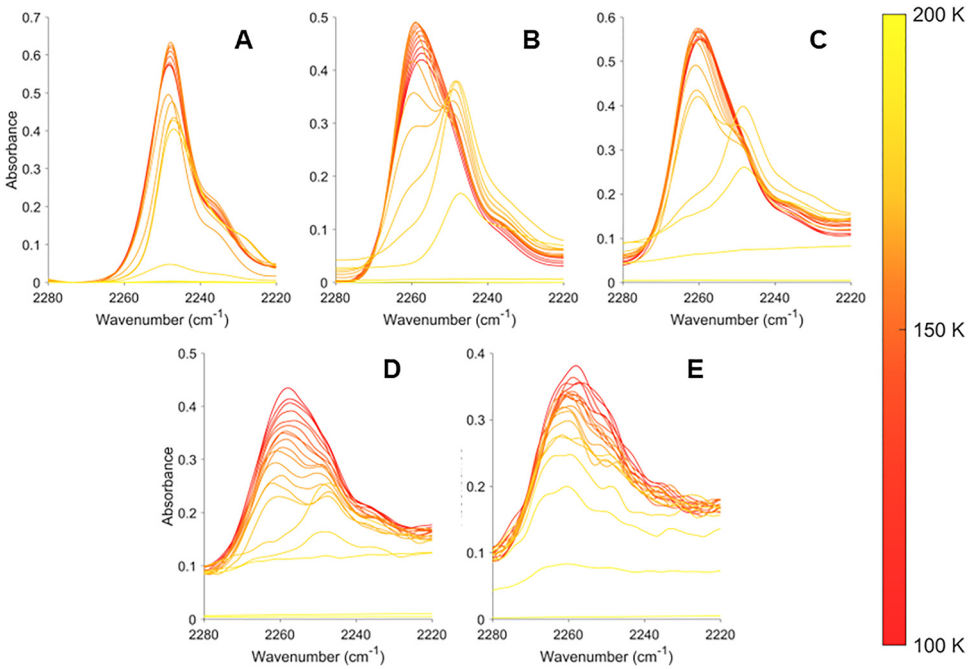

Fig. 7 RAIRS FTIR of the water-perturbed CN st. frequency (2260 cm^{-1}) and pure CN st. frequency (2247 cm^{-1}) region during ice warmup. (A: pure, B: 80 : 20, C: 50 : 50, D: 25 : 75, E: 10 : 90).

In the present study, the intensity of the water-perturbed CN stretch decreases upon warming, while the unperturbed CN stretch peak grows (Fig. 7). This is in contrast to the behavior of the CN stretch peak height within the pure ices, which decreases as the ice is warmed, likely due to temperature effects on band strength. The significant shift in our CN stretch shows a temperature dependence on the interaction between the nitrile group and the surrounding hydrogen-bond network discussed previously. The CN group appears to return to a local environment resembling that of a pure ice at elevated temperatures, where it no longer interacts strongly with the local water molecules. This behavior suggests that *n*-PrCN forms aggregates within the ice before subliming.

To further investigate this interpretation, quantum chemical calculations were performed at the ωB97X-D/6-311+G(d,p) level of theory to evaluate the binding energies of the H_2O–*n*-PrCN and *n*-PrCN–*n*-PrCN dimers. Including zero-point energy corrections, the binding energy of the H_2O–*n*-PrCN complex is 4.06 kcal mol^{-1}, whereas the *n*-PrCN–*n*-PrCN dimer is more strongly bound, with a binding energy of 6.15 kcal mol^{-1}. These results are consistent with our experimental observations and indicate that *n*-PrCN preferentially forms molecular aggregates within the ice prior to sublimation. Because the *n*-PrCN–*n*-PrCN interaction is stronger than the H_2O–*n*-PrCN interaction, the latter is thermodynamically less stable and is disrupted first upon warming. This disruption enables *n*-PrCN molecules to reorganize into more strongly bound aggregates, consistent with the observed temperature-dependent evolution of the CN stretching band, which shifts from a water-perturbed position immediately after deposition toward the characteristic CN stretch of neat *n*-PrCN upon heating.

3.6. Gas phase mm-wave detection following TPD

Building upon our *in situ* characterization of neat and mixed water ices, we now report the corresponding gas-phase detection of the desorbed molecules using broadband mm-wave rotational spectroscopy. Fig. 8 shows the TPD spectra for both conformers and all ice mixtures, and the inset shows the averaged up and down linear frequency sweep for one example condition. For each conformer, the reported trace represents the average intensity of the two rotational transitions assigned to that species. These intensities were normalized to the *gauche* conformer and corrected for the *N* abundance ratio using a scaling factor so that at the peak desorption temperature the *gauche : anti* ratio is reflected. In all these experiments, both *anti* and *gauche* conformers are detected in the primary desorption feature. However, the RAIRS data shown for neat PrCN in Fig. 2 indicate that crystallization and complete conversion to the *gauche* form has already occurred. This suggests that conformational isomerization to the *anti* form must occur either at desorption or just prior to it. Indeed, a close look at the high temperature region of the plots in Fig. 2 and 6 shows the reappearance of the *anti* species just in the temperature region corresponding to sublimation. In some of the mixed ices, full crystallization may not have occurred, but it seems in any case isomerization accompanies desorption for the main TPD peak.

We note additional details in conformer-specific desorption behavior as a function of ice composition. Increasing water content systematically shifts the primary desorption peak to lower temperatures, consistent with disruption of PrCN-PrCN interactions and substitution with weaker PrCN-H_2O interactions in mixed ices. In neat PrCN ice, intermolecular cohesion is dominated by dipole–dipole alignment and van der Waals

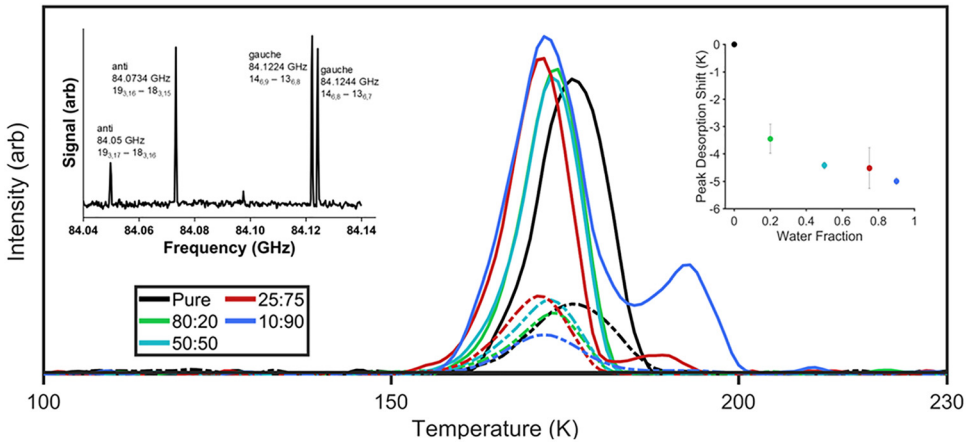

Fig. 8 TPD spectra of frequency integrated signal for the *gauche* (solid line) and the *anti* (dashed lined) following sublimation of the pure and mixed ices. TPD curves are corrected to reflect the branching ratios. The inset image (left) corresponds to the frequency region of *anti* and *gauche* used for monitoring, and the inset image (right) corresponds to the peak desorption shift from the neat for each ratio.

packing, whereas co-deposition with water inhibits formation of compact PrCN domains through hydrogen bonding and reduced packing efficiency, thereby lowering the effective desorption energy.[34–36]

In addition to the slight systematic decrease in the primary desorption temperature with increasing water content, gas-phase detection during TPD reveals the emergence of a second desorption feature at the highest water contents (25 : 75 and 10 : 90 PrCN:H_2O) that is absent in more PrCN-rich mixtures. This secondary feature coincides with the onset of water desorption and is attributed to co-desorption of PrCN molecules that become trapped within the bulk water matrix during deposition. Similar behavior has been reported previously for volatile species embedded in amorphous water ice where desorption is delayed until the amorphous-to-crystalline transition or bulk water sublimation occurs.[37,38] In the present experiments, any potential volcano desorption of PrCN alone would be obscured by the dominant desorption of neat PrCN, suggesting that the observed high-temperature feature is most consistent with water-mediated co-desorption. Independent mass spectrometric measurements of the 10 : 90 mixture confirm that the secondary PrCN sublimation event coincides with the desorption of the bulk crystalline water ice.

Interestingly, only the *gauche* conformer is detected in this secondary desorption feature. This conformer selectivity indicates that *n*-PrCN molecules trapped within the water matrix undergo conformational relaxation prior to sublimation, resulting in enrichment of the lower-energy *gauche* conformer, just as in the PrCN crystallization. Similar behavior has been observed for polycyclic aromatic hydrocarbons (PAHs) embedded in bulk water ice, where molecular reorientation toward minimum-energy configurations occurs during ice crystallization and is subsequently preserved by the rigid crystalline lattice.[39] In the case of PrCN, confinement within the water matrix likely facilitates partial conversion of the *anti* to the *gauche* form during the amorphous to crystalline transition. However, in contrast to the desorption from the PrCN-dominated peak, in this case there is no conformational isomerism accompanying any sublimation and only the *gauche* form is detected in the gas phase from the water-dominated peak.

Although these water-driven structural effects are evident in the second desorption feature, the relative conformer abundances in the first desorption feature remain largely insensitive to water content. Again, this suggests characteristic isomerization of the *gauche* form as the sublimation temperature is reached for the *n*-PrCN desorption peak. For both neat and mixed ices, only the *gauche* fraction is reported, as the *anti* conformer abundance in the second desorption feature falls below the limit of detection and precludes reliable determination of a *gauche : anti* ratio. As we reported previously for the neat *n*-PrCN, the *gauche* fraction measured in the first desorption event is greater than a 300 K Boltzmann distribution, although the effect is smaller in the present data. We

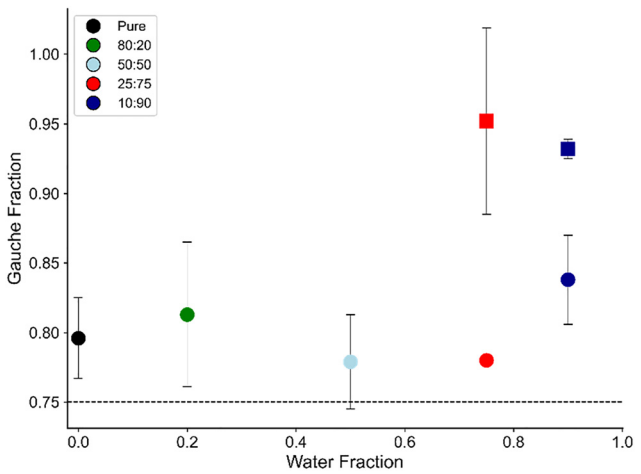

Fig. 9 *Gauche* Fraction obtained from mm-wave TPD for the first and second desorption peaks. Dotted line shows the 3 : 1 ratio from a Boltzmann distribution at 300 K. The circles represent the first desorption peak, and the squares represent the second desorption peak.

Table 1 *Gauche* fraction of the frequency integrated signal following sublimation with the peak sublimation temperature in kelvin from Fig. 8

	Neat	80 : 20 PrCN:Water	50 : 50 PrCN:Water	25 : 75 PrCN:Water	10 : 90 PrCN:Water
Gauche fraction 1st peak	0.796 ± 0.029	0.813 ± 0.052	0.779 ± 0.034	0.780 ± 0.002	0.838 ± 0.032
Gauche fraction 2nd peak	—	—	—	0.952 ± 0.067	0.932 ± 0.007
Anti T_{sub} (K)	177	175	173	171	172/193[a]
Gauche T_{sub} (K)	175	174	174	171/188[a]	173/193[a]

[a] The second desorption temperature.

attribute this difference to greatly improved S/N following incorporation of a cryogenic amplifier in our signal acquisition path. The *gauche* fraction in the first feature is consistent across all ice compositions investigated.

Fig. 9 and the corresponding Table 1 summarize the *gauche* fraction for each desorption feature along with the associated peak desorption temperatures for all mixtures studied. For neat *n*-PrCN, the *gauche* fraction in the first desorption peak is 0.79 ± 0.03, and comparable values are obtained for all mixed ices. In contrast, the second desorption features observed in the 25 : 75 and 10 : 90 *n*-PrCN:H_2O mixtures exhibit substantially higher *gauche* fractions of 0.95 ± 0.07 and 0.93 ± 0.01, respectively. These elevated values indicate strong conformer selectivity in water-rich ices, with the lower-energy *gauche* conformer preferentially retained and released during water-mediated co-desorption. As the water fraction increases, a larger proportion of *n*-PrCN molecules becomes trapped within the bulk ice, where conformational relaxation prior to desorption is facilitated. In the 25 : 75 mixture, the reduced abundance of *n*-PrCN molecules trapped within the water matrix then leads to the absence of detectable *anti* conformer signal in the second desorption feature.

These results demonstrate that water ice plays a dual role in mixed molecular ices. While the first desorption feature reflects conformer populations largely inherited from the neat system prior to crystallization, crystallization of the water-rich environments promote bulk trapping and conformational relaxation that selectively enrich the lower-energy conformer prior to co-desorption. Conformer-specific gas-phase detection enabled by CPICE provides direct insight into how ice composition and morphology govern the molecular populations which sublime.

4. Conclusion

The interactions between *n*-PrCN and water in mixed ices were investigated using RAIRS in the condensed phase and chirped-pulse mm-wave rotational spectroscopy following TPD. This combined approach yields the first experimental determination of the conformer interconversion barrier of *n*-PrCN in the condensed phase, as well as its behavior within a water-rich ice. Shifts in the CN stretching vibration at low temperature provides evidence for hydrogen-bonding interactions between *n*-PrCN and water, while the reappearance of spectral features indicative of neat *n*-PrCN at elevated temperatures indicates progressive decoupling from the water network over the course of TPD and likely formation of *n*-PrCN aggregates within the amorphous ice.

Detection by mm-wave rotational spectroscopy of molecules in the gas phase reveals that the addition of water systematically lowers the primary desorption temperature of *n*-PrCN, consistent with disruption of PrCN-PrCN cohesive interactions by the surrounding H-bonded matrix. For neat and moderately water-dilute ices, the *gauche* fraction in the first desorption event remains consistent regardless of ice composition, suggesting limited conformational equilibration during sublimation, However, in water-rich mixtures (25 : 75 and 10 : 90 *n*-PrCN:H_2O), a second desorption feature is observed coincident with crystalline bulk, in which *n*-PrCN sublimes with an increased abundance of the lower-energy *gauche* conformer. This behavior is consistent with conformational relaxation of *n*-PrCN molecules trapped within the water matrix prior to co-desorption.

These findings highlight the role of water and importance of condensed-phase structure and thermal history in shaping the conformational distributions ultimately accessible to gas-phase astronomical observations in cold astrophysical environments. Future work will systematically investigate the influence of deposition conditions, ice morphology, and isomeric composition to further constrain the condensed-phase mechanisms responsible for conformer-selective desorption.

Author contributions

E. M. Hayden: data curation (equal); formal analysis (equal); Investigation (equal); writing – original draft (equal). T. J. Hager: data curation (equal); formal analysis (equal); investigation (equal); writing – original draft (equal). R. Mata: data curation (support); formal analysis (support); investigation (support): writing (support). Q. D. Borengasser: preliminary data acquisition (support). B M. Broderick: supervision (lead); funding acquisition (equal); writing – review and editing (equal).

Conflicts of interest

The authors declare no competing interests.

Data availability

The data generated during this study are available upon request.

Supplementary information (SI) is available. See DOI: https://doi.org/10.1039/d5cp05060j.

Acknowledgements

B. M. B. gratefully acknowledges the University of Missouri for generous startup funds, and NSF Chemistry, Grant No 2414316.

References

1 J. Choi, K. Oh, H. Lee and M. Cho, *J. Chem. Phys.*, 2008, **13**, 134506.
2 S. Andrews and S. Boxer, *J. Phys. Chem. A*, 2000, **51**, 11853–11863.
3 F. Muniz-Miranda, A. Pedone and M. Menziani, *J. Comput. Chem.*, 2024, **28**, 2352–2359.
4 G. Chaban, *J. Phys. Chem. A*, 2004, **20**, 4551–4556.
5 A. Belloche, R. Garrod, H. Müller, K. Menten, C. Comito and P. Schilke, *Astron. Astrophys.*, 2009, **1**, 215–232.
6 A. Belloche, R. Garrod, H. Müller and K. Menten, *Science*, 2014, **6204**, 1584–1587.
7 J. Gabriel, E. Thoms, A. Guiseppi-Elie, M. Ediger and R. Richert, *J. Chem. Phys.*, 2022, **4**, 044501.
8 N. Ito, K. Duvvuri, D. Matyushov and R. Richert, *J. Chem. Phys.*, 2006, **2**, 024504.
9 L. Zhu and L. Yu, *Chem. Phys. Lett.*, 2010, **1**, 62–65.
10 K. Kearns, S. Swallen, M. Ediger, T. Wu and L. Yu, *J. Chem. Phys.*, 2007, **15**, 154702.
11 G. Zografi, A. Newman and E. Shalaev, *J. Pharm. Sci.*, 2025, **1**, 40–69.
12 J. Durig, B. Drew, A. Koomer and S. Bell, *Phys. Chem. Chem. Phys.*, 2001, **5**, 766–775.
13 P. Nazari, W. Rocha, A. Rubinstein, K. Slavicinska, M. Rachid, E. van Dishoeck, S. Megeath, R. Gutermuth, H. Tyagi and H. Brunken, *et al.*, *Astron. Astrophys.*, 2024, **686**, A71.
14 C. Baiano, J. Lupi, V. Barone and N. Tasinato, *J. Chem. Theory Comput.*, 2022, **5**, 3111–3121.
15 J. Cao, Z. Wang, L. Gao and F. Fu, *J. Mol. Model.*, 2015, **21**, 66.
16 R. Hudson and F. Coleman, *ACS Earth Space Chem.*, 2019, **3**, 1182–1188.
17 K. Ishii, Y. Kobayashi, K. Sakai and H. Nakayama, *J. Phys. Chem. B*, 2006, **49**, 24827–24833.
18 A. Kanaherarachchi, T. Hager, Q. Borengasser and B. Broderick, *ACS Earth Space Chem.*, 2024, **8**, 14–20.
19 S. Radhakrishnan, T. Hager, A. Kanaherarachchi, C. Williams, G. Hall and B. Broderick, *J. Chem. Phys.*, 2022, **157**, 154201.
20 T. Hager, B. Moore, Q. Borengasser, A. Kanaherarachchi, K. Renshaw, S. Radhakrishnan, G. Hall and B. Broderick, *J. Chem. Phys.*, 2024, **161**, 094201.
21 M. Rachid, W. Rocha and H. Linnartz, *Astron. Astrophys.*, 2022, **665**, A89.
22 C. Richey and P. Gerakines, *Astrophys. J.*, 2012, **759**, 74.
23 J. Fulker, M. McCoustra and W. Brown, *ACS Earth Space Chem.*, 2025, **9**, 746–756.
24 H. Müller, F. Schlöder, J. Stutzki and G. Winnewisser, *J. Molec. Struct.*, 2005, **742**, 215–227.
25 Q. Borengasser, B. Moore, K. Renshaw, M. Infante and B. Broderick, *J. Phys. Chem. Lett.*, 2025, **16**, 1660–1665.
26 K. Ishii and H. Nakayama, *Phys. Chem. Chem. Phys.*, 2014, **16**, 12073.
27 K. Ishii and H. Nakayama, *J. Non-Cryst. Solids*, 2007, **353**, 1279–1282.
28 H. Kissinger, *Anal. Chem.*, 1957, **29**, 1072–1073.
29 S. Vyazovkin, *Molecules*, 2020, **12**, 2813.
30 B. Kerkeni, V. Gamez, M. Senent and N. Feautrier, *Phys. Chem. Chem. Phys.*, 2019, **21**, 23375–23384.
31 P. Rablen, D. Miller, V. Bullock, P. Hutchinson and J. Gorman, *J. Am. Chem. Soc.*, 1999, **121**, 218–226.
32 K. Wiberg, R. Paul, J. Daniel and A. Todd, *J. Am. Chem. Soc.*, 1995, **117**, 4261–4270.
33 R. Bhuin, R. Methikkalam, B. Sivaraman and T. Pradeep, *J. Phys. Chem. C*, 2015, **119**, 11524–11532.
34 K. Eisenthal, *Chem. Rev.*, 1996, **96**, 1343–1360.
35 J. Ghosh, A. Hariharan, R. Bhuin, R. Methikkalam and T. Pradeep, *Phys. Chem. Chem. Phys.*, 2018, **20**, 1838–1847.
36 L. Yu, S. Reutzel-Edens and C. Mitchell, *Org. Process Res. Dev.*, 2000, **4**, 396–402.
37 D. Burke, A. Wolff, J. Edridge and W. Brown, *Phys. Chem. Chem. Phys.*, 2008, **10**, 4956–4967.
38 M. Collings, M. Anderson, R. Chen, J. Dever, S. Viti, D. Williams and M. McCoustra, *Mon. Not. R. Astron. Soc.*, 2004, **354**, 1133–1140.
39 A. Lignell and M. Gudipati, *J. Phys. Chem. A*, 2015, **119**, 2607–2613.